










# Modeling the mechanisms of conifer mortality under seawater exposure

Junyan Ding<sup>1</sup> , Nate McDowell<sup>1,2</sup> , Yilin Fang<sup>3</sup>, Nicholas Ward<sup>4</sup> , Matthew L. Kirwan<sup>5</sup>, Peter Regier<sup>4</sup>, Patrick Megonigal<sup>6</sup> , Peipei Zhang<sup>7</sup>, Hongxia Zhang<sup>8</sup> , Wenzhi Wang<sup>9</sup> , Weibin Li<sup>10</sup> , Stephanie C. Pennington<sup>11</sup> , Stephanie J. Wilson<sup>6</sup>, Alice Stearns<sup>6</sup> and Vanessa Bailey<sup>1</sup> 

<sup>1</sup>Biological Sciences Division, Pacific Northwest National Lab, PO Box 999, Richland, WA 99352, USA; <sup>2</sup>School of Biological Sciences, Washington State University, PO Box 644236, Pullman, WA 99164-4236, USA; <sup>3</sup>Earth Systems Science Division, Pacific Northwest National Lab, Richland, WA 99352, USA; <sup>4</sup>Marine and Coastal Research Laboratory, Pacific Northwest National Laboratory, Sequim, WA 98382, USA; <sup>5</sup>Virginia Institute of Marine Science, College of William and Mary, Gloucester Point, VA 23062, USA; <sup>6</sup>Smithsonian Environmental Research Center, Edgewater, MD 21037, USA; <sup>7</sup>CAS Key Laboratory of Mountain Ecological Restoration and Bioresource Utilization & Ecological Restoration and Biodiversity Conservation Key Laboratory of Sichuan Province, Chengdu Institute of Biology, Chinese Academy of Sciences, Chengdu 610041, China; <sup>8</sup>Shapotou Desert Research and Experiment Station, Northwest Institute of Eco-Environment and Resources, Chinese Academy of Sciences, Lanzhou 730000, China; <sup>9</sup>The Key Laboratory of Mountain Environment Evolution and Regulation, Institute of Mountain Hazards and Environment, Chinese Academy of Sciences, Chengdu 610041, China; <sup>10</sup>State Key Laboratory of Herbage Improvement and Grassland Agro-ecosystems, College of Pastoral Agriculture Science and Technology, Lanzhou University, Lanzhou 730020, China; <sup>11</sup>Joint Global Change Research Institute, Pacific Northwest National Laboratory, College Park, MD 20740, USA

## Summary

Author for correspondence:  
Junyan Ding  
Email: [junyan.ding@pnnl.gov](mailto:junyan.ding@pnnl.gov)

Received: 11 April 2023  
Accepted: 26 May 2023

*New Phytologist* (2023) **239**: 1679–1691  
doi: 10.1111/nph.19076

**Key words:** carbon starvation, hydraulic failure, plant hydraulics, root mortality, salinity, sea water exposure, tree mortality, vegetation dynamic model.

- Relative sea level rise (SLR) increasingly impacts coastal ecosystems through the formation of ghost forests. To predict the future of coastal ecosystems under SLR and changing climate, it is important to understand the physiological mechanisms underlying coastal tree mortality and to integrate this knowledge into dynamic vegetation models.
- We incorporate the physiological effect of salinity and hypoxia in a dynamic vegetation model in the Earth system land model, and used the model to investigate the mechanisms of mortality of conifer forests on the west and east coast sites of USA, where trees experience different form of sea water exposure.
- Simulations suggest similar physiological mechanisms can result in different mortality patterns. At the east coast site that experienced severe increases in seawater exposure, trees loose photosynthetic capacity and roots rapidly, and both storage carbon and hydraulic conductance decrease significantly within a year. Over time, further consumption of storage carbon that leads to carbon starvation dominates mortality. At the west coast site that gradually exposed to seawater through SLR, hydraulic failure dominates mortality because root loss impacts on conductance are greater than the degree of storage carbon depletion.
- Measurements and modeling focused on understanding the physiological mechanisms of mortality is critical to reducing predictive uncertainty.

## Introduction

Relative sea level rise (SLR) and extreme events are driving the landward retreat of coastal forests through the formation of ghost forests, or widespread swaths of dead trees (Kirwan & Gedan, 2019; Osland *et al.*, 2022). Our predictive certainty regarding ghost forest formation is poor due to a lack of understanding of the physiological processes underlying tree death from SLR, and due to the lack of vegetation dynamic models developed for shoreline ecosystems (McDowell *et al.*, 2022; Yoshikai *et al.*, 2022). Predictions are further complicated by the confounding impacts of SLR and other climate change factors such as rising atmospheric CO<sub>2</sub> levels (Chen & Kirwan, 2022a, b). Our poor capacity to predict the rate of ghost forest formation

impedes assessment and mitigation of ecosystem services and terrestrial habitat losses due to SLR (Kirwan & Gedan, 2019; Ward *et al.*, 2020). Coastal forests can be *c.* 30% more productive than adjacent inland, upland systems (Tagestad *et al.*, 2021), and these forests have larger carbon stocks than the young marshes replacing them (Smith *et al.*, 2021). Coastal forests (*i.e.* mangroves) also provide habitat for coastal fisheries and mitigate the impacts of storms and erosion.

Rising sea levels expose coastal trees to two primary threats: high salinity and hypoxia in the soil porewater, which can drive both hydraulic failure and carbon starvation (McDowell *et al.*, 2022). Hydraulic failure results from large changes in the soil-to-leaf hydraulic function. An osmotic constraint on root water uptake is the most immediate impact of increasing

porewater salinity, which acts to reduce the concentration gradient for water flow from the soil to the roots. Prolonged exposure to elevated salt concentrations will cause root damage and mortality (Robin *et al.*, 2016). Exposure to hypoxia can also impact root function and ultimately drive root mortality (Pezeshki, 2001; Flowers & Colmer, 2008). Loss of the water potential gradient as well as fine root mortality reduces belowground conductance and whole-plant hydraulic conductivity (López-Berenguer *et al.*, 2006; Nedjimi, 2014). Porewater salinity also affects xylem properties, with elevated salt promoting narrower tracheids (Wang *et al.*, 2022), and shifting embolism vulnerability of the xylem (H. Zhang *et al.*, 2021). Together, the decreasing water potential gradient, root death, and changes in xylem properties act to reduce whole-plant hydraulic conductance and increase the risk of dehydration from severe embolism, or hydraulic failure (McDowell *et al.*, 2022).

Carbon starvation is also likely under conditions of elevated salinity and hypoxia. The osmotic- and root death-induced reductions in belowground conductance as well as increases in xylem embolism drive stomatal closure and hence reduced photosynthesis (Orsini *et al.*, 2012; Sperry *et al.*, 2016). As well, increased salt concentrations inhibit potassium accumulation in guard cells, also promoting stomatal closure (Clough & Sim, 1989; Perri *et al.*, 2019). These photosynthetic constraints are exacerbated by foliar ion toxicity, in which the biochemical rate of photosynthesis is reduced due to prolonged salt exposure (Ball *et al.*, 1984; Munns, 2002; Flexas *et al.*, 2004; Suárez & Medina, 2006; Yadav *et al.*, 2011; Delatorre-herrera *et al.*, 2021; Li *et al.*, 2021). As leaf carbon balance declines, the percentage of the crown that is foliated decreases, again promoting reduced whole-plant carbon gain. The combination of the loss of stomatal conductance, photosynthetic capacity, and foliated crown drives carbon starvation as respiration continues to consume a diminishing quantity of stored carbon (P. Zhang *et al.*, 2021).

We expect that each mechanism described earlier can play a role in tree mortality, but the relative importance can vary with intensity and duration of seawater exposure, and with plant functional traits. Given that the osmotic impacts of rising porewater salinity are immediate and can be sustained (Munns & Termaat, 1986), we hypothesize that hydraulic failure is a dominant process underlying tree mortality during initial seawater exposure. We additionally hypothesize that carbon starvation increases in likelihood over time as carbohydrate stores are slowly depleted.

We used an ecosystem demography model, the functionally assembled terrestrial ecosystem simulator with plant hydraulics (FATES-Hydro) (Fisher *et al.*, 2018; Koven *et al.*, 2020), to test our hypotheses. FATES-Hydro is a physiology-based vegetation demographic model that simulates cohort-scale dynamics for different species or plant functional types. FATES-Hydro was originally developed for freshwater terrestrial ecosystems that have no salinity or water logging. Thus, we first conducted model development to introduce the physiological effects of salinity and hypoxia. We then used this new version of FATES-Hydro to investigate the importance of changing vulnerability curves and root mortality on tree mortality under different circumstances.

We conducted simulations on three coastal conifer forests: one on the Pacific coast and two on the Atlantic coast. These three sites all have extensive ghost forest formation in response to increasing seawater exposure (Wang *et al.*, 2019; Smith & Kirwan, 2021). Besides their different geography, the sites exhibit different sources of inundation. The Pacific coast site was a freshwater floodplain until 2014, after which the culverts were breached to improve fish habitat, which subsequently allowed daily tidal inundation. This ‘manipulative’ study site contrasts with those on the Atlantic coast, which are exhibiting ghost forest formation that is accelerating in parallel with increasing rates of relative SLR (Schieder & Kirwan, 2019). The Pacific coast site was used for extensive evaluation of the mechanisms underlying seawater-induced mortality, with additional evaluation and simulation of mortality at the two Atlantic sites. Across all sites, we investigated the role of seawater exposure and the variation of tree functional traits on the likelihood of mortality.

## Materials and Methods

### Study area

The first site is a *c.* 100-yr-old Sitka-spruce forest in the Beaver Creek (BC) watershed (a tributary of Johns River, which drains into the Grays Harbor estuary; 46°54'N, 123°58'W) at the Pacific coast in western Washington State, USA (Li *et al.*, 2021; H. Zhang *et al.*, 2021; P. Zhang *et al.*, 2021; Wang *et al.*, 2022). The climate is dominated by warm, dry summers and cool, wet winters. Before 2014, the shoreline forest on the floodplain was protected from seawater incursion by a causeway. The barrier was removed in November 2014, allowing the previously freshwater ecosystem to be exposed to tidal water levels and salinities from the Grays Harbor estuary, with tidal inundation driving groundwater salinization (Yabusaki *et al.*, 2020; Regier *et al.*, 2021). This led to mortality of the spruce trees, which was a function of elevation above sea level (H. Zhang *et al.*, 2021; P. Zhang *et al.*, 2021). While tidal swamps exist in the Pacific Northwest with Sitka-spruce trees that can sustain flooding and salinity (Kauffman *et al.*, 2020), this diked system developed under conditions more akin to upland conditions, similar to the other sites we assess in this study. Soil pore water salinity, crown area, carbohydrates, growth, sap flow, and leaf physiological variables have been reported for the dying trees at this site. Measured leaf physiological variables include the maximum rate of Rubisco carboxylase activity ( $V_{cmax}$ ) and the maximum rate of photosynthetic electron transport ( $J_{max}$ ), leaf water potential, carbon fixation rate, and transpiration rate (details of the field measurements can be found in Li *et al.*, 2021; H. Zhang *et al.*, 2021; P. Zhang *et al.*, 2021; Wang *et al.*, 2022). Seasonal and spatial soil salinity variation was simulated from 2014 to 2019 over the watershed (Yabusaki *et al.*, 2020).

The second and third sites (Goodwin Island (GWI) and Moneystump (MS)) are located in the Chesapeake Bay region of the U.S. mid-Atlantic coast (38.5°N, 76.3°W) (Smith & Kirwan, 2021). The climate there is characterized by hot, humid summers and cool winters. The Chesapeake Bay region is a hotspot for sea-

level-driven coastal forest retreat, driven by rapid SLR across a gently sloping coastal plain topography (Schieder *et al.*, 2018; Chen & Kirwan, 2022a,b). The 20<sup>th</sup> century relative SLR rates in the Chesapeake Bay region (*c.* 3–6 mm per year) are approximately two to three times faster than the global average (Ezer & Corlett, 2012; Sallenger *et al.*, 2012). Both GWI and MS are dominated by loblolly pine (*Pinus taeda*) forests. Rapid SLR in recent decades has led to extensive tree mortality at the shoreline (low elevation) locations, which are periodically exposed to saline water, while the neighboring uplands are only influenced by saline water during large storms. Though the two Chesapeake Bay sites are similar, GWI has experienced a higher SLR rate (8.77 mm yr<sup>-1</sup>) than MS (6.84 mm yr<sup>-1</sup>) (<https://tidesandcurrents.noaa.gov/sltrends/sltrends.html>, <https://www.star.nesdis.noaa.gov/socd/lisa/SeaLevelRise/>). At GWI and MS, measurements of soil salinity were made in June of 2019, 2020, and 2021 at varying elevations (Smith & Kirwan, 2021). There is also ongoing continuous measurements at GWI and MS that started in April 2022.

## FATES-Hydro and model development

**Description of FATES-Hydro** FATES is a cohort-based, size-structured dynamic vegetation model where long-term plant growth, mortality rates, and competition emerge as a consequence of physiological processes. FATES has been coupled with both the COMMUNITY LAND MODEL v.5 (CLM5) (Lawrence *et al.*, 2019) and the land surface model (ELM) component of the Energy Exascale Earth System Model (Golaz *et al.*, 2022). In this study, FATES is coupled with ELM. FATES-Hydro is a recent development of the FATES model (Fisher *et al.*, 2018; Koven *et al.*, 2020), in which a plant hydro-dynamic module, originally developed by Christoffersen *et al.* (2016), was coupled to the existing photosynthesis and soil hydrology modules. Later we give a brief introduction to FATES-Hydro. Details of FATES and the hydraulic module can be found in the technical notes (<https://fates-users-guide.readthedocs.io/projects/tech-doc/en/latest/index.html>).

In FATES-Hydro, the total transpiration of a plant is the product of total leaf area and the transpiration rate per unit leaf area ( $J$ ), which itself is the product of the difference in intercellular leaf vapor pressure, ambient vapor pressure, and stomatal conductance. For each plant cohort, the hydro-dynamic module approximates the water flow through a plant's root, xylem, and leaf systems as flow through variably saturated porous media (Sperry *et al.*, 1998) with conductance and capacitance changing in response to stem water potentials dictated by the pressure–volume ( $P$ – $V$ ) curve and the pressure–conductance (vulnerability) curve (Manzoni, 2014; Christoffersen *et al.*, 2016).

Stomatal conductance is modeled in the form of the Ball–Berry conductance model (Ball *et al.*, 1984; Oleson *et al.*, 2013; Fisher *et al.*, 2018) with a further constraint of leaf water potential through a water stress index  $\beta_p$ , defined by a function of the ratio of the leaf water potential to the leaf water potential of half stomatal closure ( $P_{50g}$ ) (Christoffersen *et al.*, 2016). The soil column is divided into a given number of layers. The proportion of roots in each layer is calculated from Zeng's (2001) two-parameter

power law function. Water flow from each soil layer within the root zone into the plant root system is calculated as a function of the hydraulic conductance determined by root biomass and root traits such as specific root length, and the difference in water potential between the absorbing roots and the rhizosphere.

**Major model developments** FATES-Hydro was originally developed for freshwater-dominated, upland ecosystems. Here we implemented mechanisms of the physical and physiological effects of salinity and hypoxia in FATES-Hydro. We give a brief description of the major developments later, with the details and formulas provided in Supporting Information Methods S1.

In the current FATES-Hydro model, osmotic potential is not included in soil hydrology. We introduced a new routine to read daily soil salinity data (in PSU: practical salinity unit or parts per thousand) into the plant hydraulic module. We introduce a root salt exclusion function that links the salinity of plant organs (root, stem, and leaf) to soil salinity through a linear function. Salinity is then converted into osmotic potential.

The photosynthetic capacity of the leaf is linked to leaf salinity using a logistic function. The parameters of the function are estimated through the best fit to field observations (Fig. S1a), in which photosynthetic capacity declined significantly with increasing salinity (Li *et al.*, 2021). Field observations from previous work at BC showed that the shape of the embolism vulnerability curves change with soil salinity (H. Zhang *et al.*, 2021). In the current plant hydraulic module, embolism vulnerability curve parameters are constant over time. We introduce a new function that modifies the parameters of the vulnerability curve assuming that the parameters change with salinity at a constant rate. Thus, the shape of the curve changes with xylem salinity (Fig. S1b). The parameters and their change rates with respect to salinity are fitted to observed patterns (H. Zhang *et al.*, 2021). Note that in this development plant physiological properties respond to soil salinity instantaneously because photosynthetic capacity and the embolism vulnerability curves are direct functions of salinity.

Previous studies have shown loss of root conductance in saline and/or waterlogged soil either due to root loss (Pezeshki *et al.*, 1996) and inhibition of aquaporin activity in the root membranes (Aroca *et al.*, 2011). In FATES-Hydro, root conductance is calculated from total root biomass. Here we introduce a root reduction function that downscales the total fine root biomass by the two stress terms: hypoxia stress and salinity stress are controlled by both the duration and intensity of salinity (or degree of saturation) (Eqns S7, S8). Note, here we do not have data of the degree of soil saturation. But, at our sites, hypoxia and soil salinity are highly coupled because both of them are the result of sea water flooding. Thus, we use the salinity term to capture the root mortality from both hypoxia and salinity in this study. Fig. S1(c) shows the percentage reduction of fine root biomass with the dimensionless stress term.

## Numerical experiment design

We conducted two sets of simulations at three sites. First, we conducted simulations of the shoreline and upland ecosystems with

all the mechanisms active. Second, to investigate the effect of root mortality and changing vulnerability curves, we conducted simulations only at the shoreline location of each site, with root mortality and changing vulnerability curves deactivated independently.

We use the University of East Anglia Climatic Research Unit (CRU) Japanese Reanalysis (JRA) meteorological product (CRUJRA) (University of East Anglia Climatic Research Unit & Harris, 2019) to drive the model. We conducted a 10-yr (2010–2019) run at BC and 30-yr (1990–2019) run at GWI and MS. The simulations are initialized with tree inventory data (DBH of all the trees in a 30 m × 30 m plot) from each site.

For BC (west coast site), we used the modeled daily soil salinity from Yabusaki *et al.* (2020) at 22 individual tree locations from the lowest elevation location (shoreline) to the highest elevation location (upland), where the salinities at shoreline and upland are shown in Figs 1(a) and S2(a). For GWI and MS, there are no long-term daily soil salinity data available; however, there are spot measurements of soil salinity at different topographic positions for both sites from 2019, 2020, and 2021 (Smith & Kirwan, 2021). Note, the shoreline locations of GWI and MS are corresponding to the transition zone in spot measurements (Smith & Kirwan, 2021). Soil salinity at the shoreline is caused by flooding of sea water, and is affected by its vertical distance to the typical tidal height (e.g. meters above mean height of high water (MHHW)) and the sea water salinity. The point measurements of soil salinity show a good relationship with the relative distance of the location to the mean tidal height at both GWI and MS, expressed by a quadratic equation (Fig. S2d,e; Eqn S8). The shoreline location that is

currently *c.* 0.24 m above MHHW would be farther from MHHW in earlier times when sea level was low. So, we estimated the distance to MHHW of the shoreline location,  $h_{SH}(t)$ , for previous years using the SLR rate. Then, we obtained the open-water salinity to capture the seasonal variation of soil salinity. We obtained the open water salinity of the stations that are close to each site (Fig. S2b,c) (Maryland Department of Natural Resources, Eyes on the Bay: <https://eyesonthebay.dnr.maryland.gov/>). At MS, we set to equal the soil salinity at height, that is, 0.24 m,  $S_{0.24}(t)$ , above MHHW to the open water salinity of the nearby station because soil salinity at that height from spot measurements matches well with open water salinity in those 3 yr (at GWI, we subtract 10 PSU from open water salinity). We then estimated the daily soil salinity values of the study period (1990–2019) at the shoreline locations of the two Chesapeake Bay sites (Fig. 2b,c) from  $h_{SH}(t)$  and  $S_{0.24}(t)$  using Eqn S9(d) (See Methods S2 for derivation). Note: there is a period in 2019 when the stations had no measurements of the open water salinity and thus the estimated soil salinity during that period might not accurately represent the soil salinity at the sites.

To check how well the soil salinity at the shoreline locations was estimated by our empirical methods, we compared the measured soil salinity of the growing season in 2022 of the shoreline locations at MS and GWI with the estimated soil salinity by the empirical method based on open water salinity at the nearby stations (Fig. S3). The matches are reasonable. Therefore, the empirical estimated soil salinity at the shoreline location of MS and GWI was able to catch the general pattern of the variation of soil salinity over the simulation period.

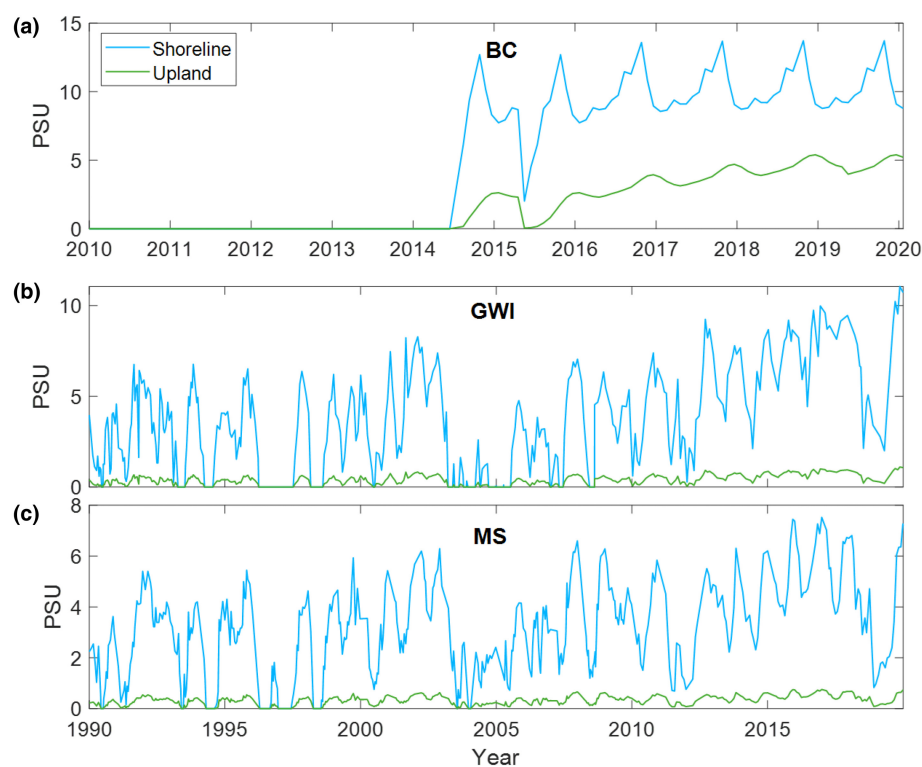


**Fig. 1** Mean daily soil salinity of the shoreline and upland forests at (a) Beaver Creek (BC), (b) Goodwin Island (GWI), and (c) Money Stump (MS). PSU, practical salinity unit in part per thousand.

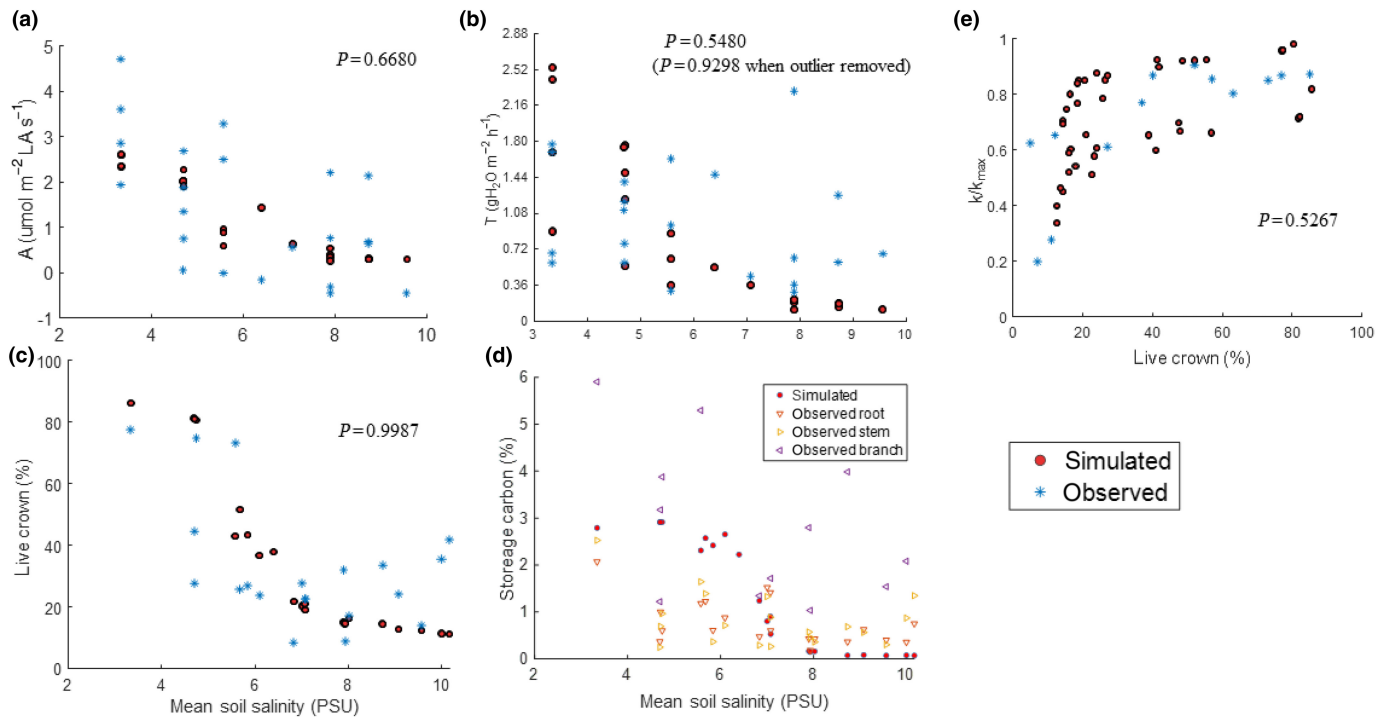


**Fig. 2** Simulated and observed relationships between soil salinity and (a) mean daily photosynthesis per leaf area ( $A$ ), (b) mean daily transpiration rate per leaf area ( $T$ ), (c) % live crown, (d) % non-structural carbon (NSC), and (e) relation of relative (proportion of maximum) xylem conductivity ( $k/k_{\max}$ ) and % live crown, over the 2019 growing season at Beaver Creek.

### Parameterization, calibration, and benchmarking

When field observations were not available, the main parameters used in FATES-Hydro (Table 1) are estimated from field observations at BC or obtained from the TRY trait database (Kattge *et al.*, 2011). The leaf-level parameters for photosynthetic capacity were estimated by fitting a sigmoidal function of observed values and corresponding soil salinity. The stomatal parameters of  $g_s$  and  $P50g_s$  were estimated based on stomatal conductance observations at BC (H. Zhang *et al.*, 2021; P. Zhang *et al.*, 2021). The allometry parameters that define the relations between height, sapwood area, total woody biomass, and diameter at breast height are estimated based on values of the Biomass and Allometry Database (BAAD) (Falster *et al.*, 2015). Then, leaf biomass to allometry parameters were calibrated based on observed breast height diameters and an allometric equation for Sitka spruce so that the site-level canopy LAI matches estimated non-defoliated (pre-seawater exposure) LAI of  $4.2 \text{ m}^2 \text{ m}^{-2}$  (Li *et al.*, 2022) based on the formula by Tobin *et al.* (2006). We adjusted the respiration rate so that the trees maintain full crown and the growth rate matches the observed rate (Wang *et al.*, 2022) during the pre-dam removal period.

The root mortality parameters are calibrated by matching simulated relations of  $k/k_{\max}$  and transpiration with soil salinity to observed relations of the growing season of 2019 (Fig. 2b,e). The root salt exclusion ratio ( $k_{\text{ex}}$ ) was set to 0.8 based on the observed relationship between leaf and soil ion concentrations (H. Zhang *et al.*, 2021; P. Zhang *et al.*, 2021).

Total mortality in the model is the sum of carbon starvation mortality and hydraulic failure mortality. Carbon starvation mortality rate increases with depletion of non-structural (storage) carbon (NSC) and hydraulic failure mortality rate increases with loss of xylem conductivity ( $k/k_{\max}$ ), both of which reach the maximum rates when storage carbon and xylem conductivity become zero (see FATES tech notes for detail). The parameters that control the mortality rates are estimated from the observed % NSC, percentage loss of xylem conductance, and time to death at the BC site.

For benchmarking, we compared the changes of simulated carbon fixation, transpiration, % live crown, %NSC with mean soil salinity as well as the relation between % live crown and  $k/k_{\max}$  of the growth season of 2019 with observed patterns at BC. We ran a paired-sample *t*-test to test the statistical significance of similarity between simulated and observed patterns, except for %NSC which we inspected visually. The calibrated parameters are used for the simulations at all three sites. We assumed that the conifers at MS and GWI had similar traits to the trees at the BC site. We have compared the values of these traits of the conifers in the TRY database and the allometry relations in the BAAD database; they are all very similar. We also obtained  $V_{\text{cmax}}$ , SLA values from leaf samples at the MS site, which overlap with the ones of BC (Fig. S4). These data support our assumption.

### Results

The simulated relationships at BC between % mean daytime photosynthesis, transpiration, % live crown, non-structural

**Table 1** List of major parameters within FATES-Hydro.

Symbol	Source code name	Value	Units	Description	Source
P50gs	fates_hydr_p50_gs	-2.0	MPa	Leaf xylem water potential at half stomatal closure	Wang <i>et al.</i> (2022)
$a_{gs}$	fates_hydr_avuln_gs	5	Unitless	Shape parameter for stomatal closure	Wang <i>et al.</i> (2022)
$k_{max}$	fates_hydr_kmax_node	0.7	kg MPa <sup>-1</sup> ms <sup>-1</sup>	Maximum xylem conductivity per unit sap area	This study
A	fates_hydr_vg_alpha_node	0.198392	Mpa <sup>-1</sup>	Shape parameter of van Genuchten plant hydraulic model when soil PSU = 0	This study
$m, n$	fates_hydr_vg_m_node fates_hydr_vg_n_node	0.866, 2.765	Unitless	Shape parameter of van Genuchten plant hydraulic model when soil PSU = 0	This study
dA, dn	fates_hydr_vg_da_sal fates_hydr_vg_dn_sal	-0.00651 -0.122193	Unitless	Change in A and n of plant hydraulic model per unit PSU	This study
X	fates_hydr_p_taper	0.333	Unitless	Xylem taper exponent	Christoffersen <i>et al.</i> (2016)
RWC <sub>res,lr</sub> , RWC <sub>res,sr</sub> RWC <sub>res,r</sub>	fates_hydr_resid_node	0.25, 0.325, 0.15	Proportion	Residual fraction of leaf, stem, root	Christoffersen <i>et al.</i> (2016)
$\Theta_{sat,x}$	fates_hydr_thetas_node	0.65	cm <sup>3</sup> cm <sup>-3</sup>	Saturated water content of xylem	Christoffersen <i>et al.</i> (2016)
SLA <sub>max</sub> SLA <sub>top</sub>	fates_leaf_slamax fates_leaf_slatop	0.014 0.014	m <sup>2</sup> gC <sup>-1</sup> m <sup>2</sup> gC <sup>-1</sup>	Maximum specific leaf area (SLA) SLA at top of canopy, projected area basis	This study This study
$V_{C_{max,25,top}}$ (PSU = 0)	fates_leaf_vcmax25top	50	μmol CO <sub>2</sub> m <sup>-2</sup> s <sup>-1</sup>	Maximum carboxylation rate of Rub. at 25C, canopy top	This study
$g_o$ kg	fates_leaf_stomatal_intercept fates_leaf_stomatal_slope	10 000	μmol H <sub>2</sub> O m <sup>-2</sup> s <sup>-1</sup>	Minimum leaf stomatal conductance	This study
ra, rb	fates_fnrt_prof_a fates_fnrt_prof_b	0.6, 1	Unitless	Root distribution parameters	This study
$k_{ex}$	fates_hydr_k_salex	0.80	Ratio	Root salt exclusion ratio	This study
$k_{sal}$	fates_hydr_frt_loss_salk	0.0000075	Unitless	Salinity root loss rate par.	Calibrated
$cr_{sal}$	fates_hydr_frt_loss_salcr	3.5	PSU	Salinity root loss threshold	Calibrated
$m_{cs}$	fates_mort_scalar_cstarvation	1.2	NN <sup>-1</sup> yr <sup>-1</sup>	Maximum carbon starvation mortality rate	This study
$m_{hf}$	fates_mort_scalar_hydrfailure	1.2	NN <sup>-1</sup> yr <sup>-1</sup>	Maximum hydraulic failure mortality rate	This study

carbohydrates, and mean soil salinity were all consistent with observed patterns as indicated by large  $p$  values (Fig. 2a–d,  $P = 0.6680, 0.9298, 0.9987$ ) (Note, large  $P$  value means the different between the two datasets are not significant. The larger the  $P$  value, the more similar the two datasets). In addition, the relation of relative (proportion of maximum) xylem conductivity and % live crown captured the observed patterns well (Fig. 2e,  $P = 0.5267$ ).

Given the strong benchmarking results, we had confidence in using the model to examine the processes that lead to tree mortality. To do this, we examined the time series of state variables at three levels: leaf properties (gross primary production (GPP), transpiration  $E_T$ , and stomatal conductance  $g_s$ ), whole-plant properties (% live crown, %NSC,  $k/k_{max}$ , leaf water potential  $\Psi_{leaf}$ ), and demographic properties (growth and mortality), of shoreline and upland forests at the BC, GWI, and MS sites. Note that because the open water salinity data for GWI and MS has a large gap in 2019, we only present the outcomes of aforementioned variables for those two sites from 1990 to 2018.

At BC, the leaf GPP,  $E_T$ , and  $g_s$  of shoreline trees rapidly dropped to near zero in the first year after seawater exposure, with

a much slower decline for the trees located in the upland areas where seawater exposure was less severe (Fig. 3a–c). At GWI and MS, three time periods of variation in leaf level variables emerged. Before 2007, the GPP,  $E_T$ , and  $g_s$  of shoreline and upland trees are similar. From 2007 to 2015, GPP and  $E_T$  of shoreline trees gradually drifted downwards. In 2015, there is a dramatic drop in GPP,  $E_T$ , and  $g_s$  for the shoreline trees. GPP and  $E_T$  of upland trees remain more or less the same over the whole simulation period (Fig. 3d–j).

The whole-tree variables we investigated showed similar results to those at the leaf level. At BC, the % live crown, %NSC,  $k/k_{max}$  (Fig. 4a–c), and  $\Psi_{leaf}$  (Fig. S5b) of shoreline trees began dropping in 2015 and approached zero by the end of 2019. By contrast, these variables showed relatively little change for the upland trees, with only slight drop of  $k/k_{max}$  and  $\Psi_{leaf}$  in the last 2 yr. At GWI and MS, the % live crown, %NSC,  $k/k_{max}$ , and LWP of upland trees remained at the same level over the entire 30 yr (Figs 4d–i, S5b). The % live crown, %NSC,  $k/k_{max}$ , and  $\Psi_{leaf}$  of shoreline trees are similar to those of upland trees before 2000. From 2000 to 2013, the % live crown and  $k/k_{max}$  of shoreline trees dropped slightly, followed by a significant drop after 2013 (Figs 4d–i,

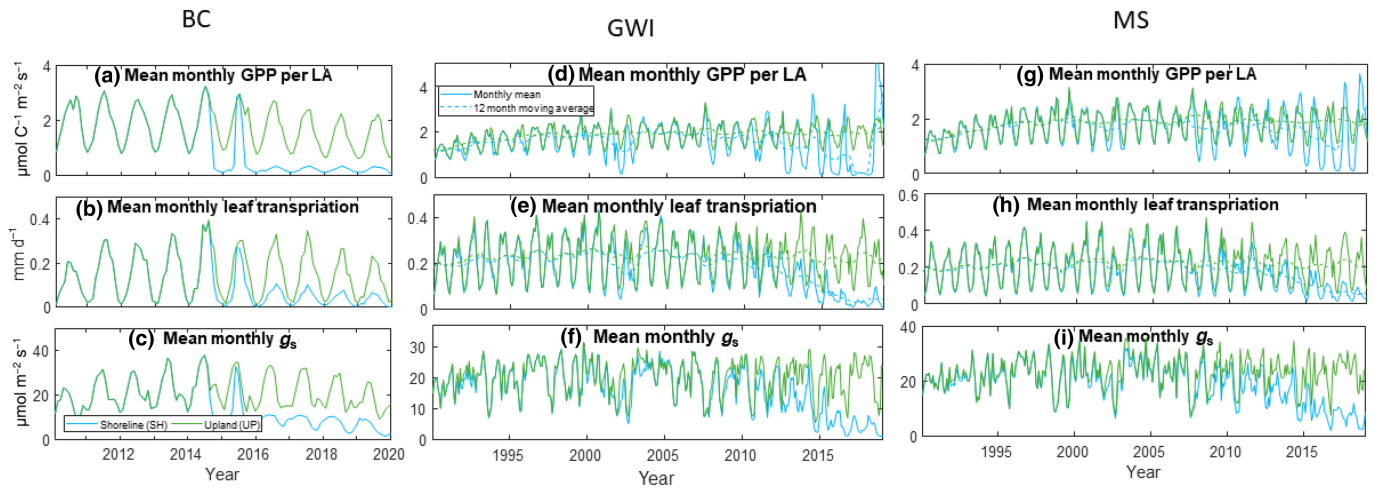


**Fig. 3** Monthly means of leaf-level physiology of three sites: mean photosynthetic rate (GPP) per leaf area at (a) Beaver Creek (BC), (d) Goodwin Island (GWI), and (g) Money stump (MS); mean monthly transpiration rate at (b) BC, (e) GWI, and (h) MS; and mean monthly stomatal conductance ( $g_s$ ) at (c) BC, (f) GWI, and (i) MS. Dashed lines are the 12-month moving averages showing the general trends at the GWI and MS sites.

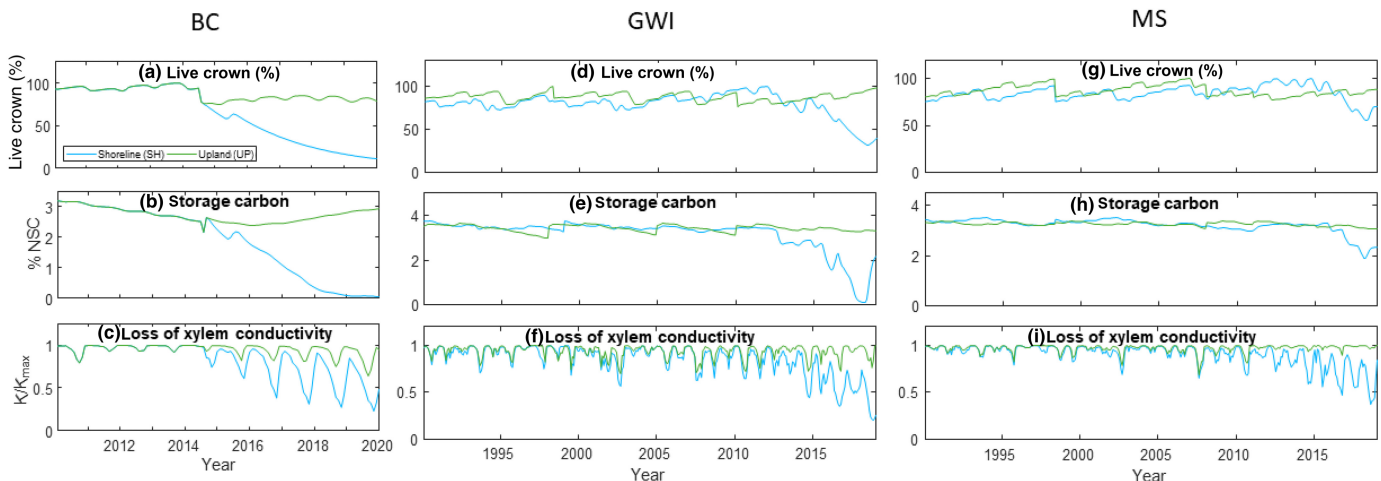


**Fig. 4** Monthly means of whole plant state variables: mean monthly % live crown (a) Beaver Creek (BC), (d) Goodwin Island (GWI), and (g) Money stump (MS); mean monthly % non-structural carbon (NSC) at (b) BC, (e) GWI, and (h) MS; (c) mean monthly loss of xylem conductivity ( $k/k_{max}$ ) at (c) BC, (f) GWI, and (i) MS.

S5b). The %NSC and  $\Psi_{leaf}$  of shoreline trees did not drop until 2015 (Figs 4e, S5b).

Simulated mortality and growth were strongly related to seawater exposure at all three sites. At BC, mortality increased dramatically after 2015 in the shoreline trees (Fig. 5a). Hydraulic failure and carbon starvation evenly contributed to mortality of shoreline trees during the first 2 yr after 2015, but carbon starvation became the major cause in later years, at which time it contributed to *c.* 70% of tree mortality (Fig. 5b). The upland trees show a much slower increase in mortality since 2015. Growth rates (basal area increment normalized by basal area; BAI/BA) of shoreline trees quickly dropped to zero within 1 yr of inundation exposure (Fig. 5b).

The simulated mortality rate of shoreline trees at GWI increased after 2013. The model predicted that hydraulic failure was the dominant process underlying mortality before 2015, after which carbon starvation became more important (Fig. 5c).

Simulated growth of shoreline trees decreased to near zero after 2015 (Fig. 5d). The shoreline trees at MS exhibited increasing mortality after 2010, driven primarily by hydraulic failure (Fig. 5e). Simulated growth of the shoreline trees was similar to those of the upland trees before 2008 after which growth declined rapidly (Fig. 5f). These patterns are consistent with the observed growth patterns at the two sites. The simulated growth rates at GWI are close to observed values, but simulated growth rates at MS are overall higher than observed rates.

To further investigate the mechanisms underlying mortality, we examined the variable time series of the shoreline trees at all three sites with root mortality and changing vulnerability curve turned on or off. That is, we deactivated root death and changing vulnerability curve one-by-one to examine the impact of these two mechanisms on mortality. We also conducted these sensitivity analyses in the upland forests, but found the impacts on mortality were trivial and similar across all scenarios because seawater

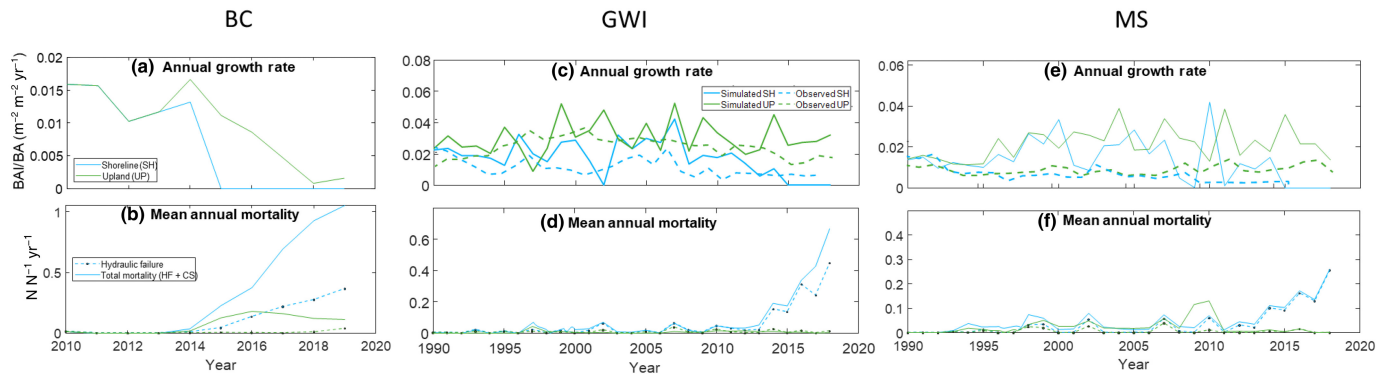


**Fig. 5** Demographic processes: annual growth rate (basal area increment normalized by basal area (BAI/BA)) at (a) Beaver Creek (BC), (c) Goodwin Island (GWI), and (e) Moneystump (MS); and annual total mortality and hydraulic failure mortality risk ( $N N^{-1} yr^{-1}$ ) at (b) BC, (d) GWI, and (f) MS.

inundation is limited in the uplands; for this reason, we do not present results from the upland simulations. Here we refer to R.M. as only root mortality being active, C.V. as only changing vulnerability curve being active, R.M. + C.V. as both mechanisms being active (this is the case presented in previous section), and Null as both mechanisms being inactive.

At BC, MS, and GWI, the variables  $k/k_{max}$ ,  $g_s$ ,  $E_T$ ,  $\Psi_{leaf}$ , and mortality rate exhibited differences between the four parameter settings. By contrast, there was no significant difference in GPP, % live crown, %NSC, and growth rates among different parameter settings (Figs 6, 7). As compared to the Null case, R.M. alone affects the physiological traits, and growth and mortality of the shoreline trees of all three sites in similar ways, but differs in the magnitude over time. At BC, R.M. results in lower  $g_s$ ,  $\Psi_{leaf}$  (Fig. 6b,c), and  $k/k_{max}$  (Fig. 7b). As compared to the Null case, R.M. alone slightly increases total mortality and hydraulic failure mortality from 2015 to 2019. At GWI and MS, R.M. alone reduces  $g_s$ ,  $\Psi_{leaf}$  (Fig. 6b,f,h,i), and  $k/k_{max}$  (Fig. 7e,h) around 2012, which becomes more significant after 2015. Unlike BC, at GWI and MS, R.M. greatly increases the total mortality and hydraulic failure mortality.

As compared to the Null case, C.V. alone has a negligible effect on  $g_s$  and  $\Psi_{leaf}$  (Fig. 6b,c,e,f,h,i) at all three sites. At BC, C.V. alone results in much lower  $k/k_{max}$  (Fig. 7b) starting in 2016. The loss of  $k/k_{max}$  from C.V. alone is higher than that from R.M. alone in (2016 and 2017) and becomes similar at the end of simulation period. At GWI, C.V. alone results in slightly lower  $k/k_{max}$  after 2015, but has no noticeable effect on  $k/k_{max}$  at MS. At all three sites, C.V. alone has little impact on mortality rates.

R.M. + C.V. affect the physiological traits and growth and mortality of the shoreline trees of all three sites in similar ways, but they differ in the variation of magnitude over time. At BC, R.M. and C.V. result in lower  $g_s$  and  $\Psi_{leaf}$  (Fig. 6b,c) starting 2016, which is similar to the effects of R.M. alone. But R.M. + C.V. results in much lower  $k/k_{max}$  ( $< 0.5$ , Fig. 7b) at BC since 2015. R.M. + C.V. greatly increase iWUE since 2015 (Fig. S6a) in the same magnitude as R.M. alone. R.M. + C.V. result in higher hydraulic failure mortality and increases by *c.* 30% the total mortality at BC from 2015 to 2019 (Fig. 7c). At GWI and MS, R.M. + C.V. have exactly the same effect on  $g_s$  and  $\Psi_{leaf}$  as R.M. alone, both of which start to slightly decrease around 2012

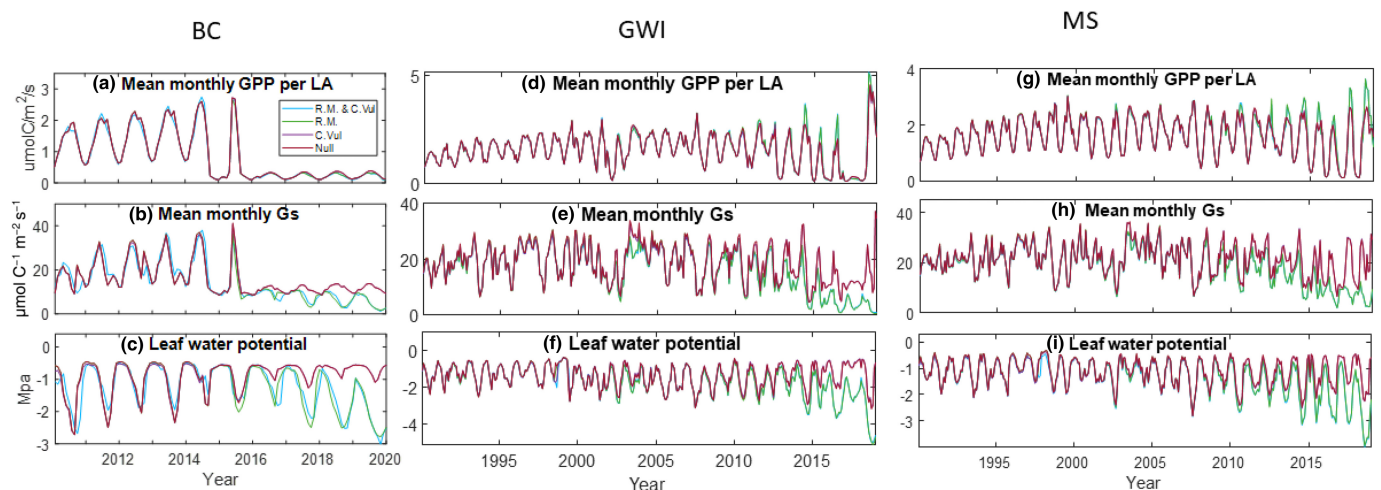


**Fig. 6** Effects on the leaf level physiology of shoreline forest with root mortality (R.M.) and change of vulnerability curve (C. Vul) turned off one-by-one. Mean monthly photosynthetic rate per leaf area (LA) at (a) Beaver Creek (BC), (d) Goodwin Island (GWI), and (g) Moneystump (MS); mean monthly stomatal conductance ( $G_s$ ) at (b) BC, (e) GWI, and (h) MS; and mean monthly leaf water potential at (c) BC, (f) GWI, and (i) MS.



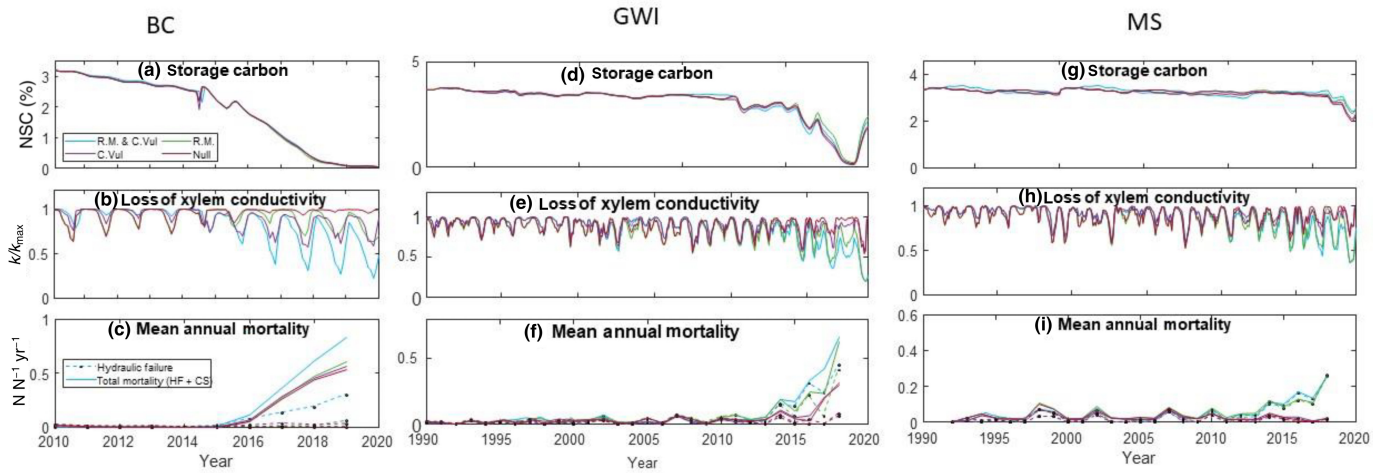


**Fig. 7** Effects of the whole plant level responses of the shoreline forests with root mortality (R.M.) and change of vulnerability curve (C. Vul) turned off one-by-one. Mean monthly % nonstructural carbon (NSC) at (a) Beaver Creek (BC), (d) Goodwin Island (GWI), and (g) Moneystump (MS); mean monthly loss of xylem conductivity at (b) BC, (e) GWI, and (h) MS; and annual total mortality and hydraulic failure mortality risk at (c) BC, (f) GWI, and (i) MS.

and become more significant after 2015 (Fig. 7b,f,h,i). At GWI, R.M. + C.V. result in much lower  $k/k_{max}$  since 2015 as compared to R.M. alone (Fig. 7e,h), whereas at MS R.M. + C.V. result in loss of  $k/k_{max}$  since 2012 of the same magnitude as R.M. alone. R.M. + C.V. result in increase of iWUE since 2010 at both GWI and MS. At GWI, R.M. + C.V. result in higher total mortality and hydraulic failure mortality than R.M. alone from 2014 to 2018, but causes the same mortality rates as R.M. alone in 2018. At MS, the effect of R.M. + C.V. is exactly the same as R.M. alone.

## Discussion

In this study, we modified FATES-Hydro to represent the plant hydrodynamic response to seawater inundation and applied the model to investigate the mechanisms of coastal forest mortality. This is the first application of FATES-Hydro for coastal settings exposed to seawater. The simulated relationships between physiological variables and soil salinity from BC matched well with observations (Fig. 2). We subsequently ran the model under two very different salinity conditions: a sudden dramatic jump from 0 to  $c. 12$  PSU in 2 yr at BC, and a gradual increase of 3 PSU over 30 yr at GWI and MS (Fig. 1). Thus, the shoreline forest at BC experienced sudden extreme stress, whereas the shoreline forests at GWI and MS experienced prolonged, chronically increasing but more modest levels of stress. The trajectory of the diagnostic plant variables suggests that the salinity scenarios at the three sites control the magnitude and time scale of change in leaf level traits (Fig. 3) and root mortality rates (indicated by Figs 6, 7) that result in loss of crown, NSC, and xylem function (Fig. 4) at different rates. Consequently, growth and mortality change in different ways at BC, GWI, and MS over the simulation periods (Fig. 5). Therefore, the same mechanistic responses to soil salinity and hypoxia lead to different total mortality rates and alter the relative importance of carbon starvation and hydraulic failure at the three sites (Fig. 8).

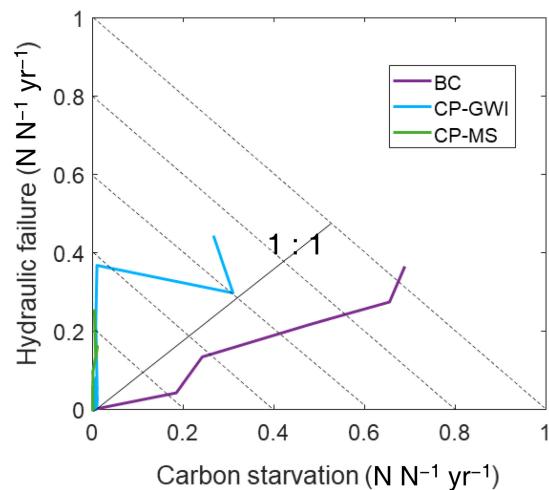


**Fig. 8** Simulated mortality patterns of Beaver Creek (BC), Goodwin Island (GWI), and Moneystump (MS). Black dashed lines are isolines of total mortality rate, and the solid black line is the 1 : 1 ratio line on which hydraulic failure and carbon starvation contribute equally to total mortality.

The simulated leaf GPP,  $E_T$ , and  $g_s$  (Fig. 3) of shoreline forests are all lower than those of upland forests at the three sites. The simulated reduction in leaf GPP and  $E_T$  agree with the findings of other modeling studies (Li *et al.*, 2022; Yoshikai *et al.*, 2022) and field observations (Duberstein *et al.*, 2020; Pan *et al.*, 2020) of coastal forests. Our model also shows soil salinity can lower leaf water potential,  $\Psi_{leaf}$ , by as much as 2 MPa (Fig. S5). This large magnitude of impact has also been observed in field studies (Nishida *et al.*, 2009; Qin *et al.*, 2010).

Our study reveals that the rate of change in leaf-level physiology varies with salt and flood exposure history. The rate of decline of these leaf-level variables was rapid at BC where the rise in salinity and inundation was rapid and of large magnitude (Fig. 1). At BC, salt toxicity and root reduction occur in parallel. Due to limited root salt exclusion, high salt concentrations in

leaves are achieved and consequently enzyme degradation occurs (Sudhir & Murthy, 2004). Meanwhile, rapid root loss forces stomatal closure through reduced belowground conductance (Fig. 3c). At GWI and MS, these processes occur more gradually and at different timescales due to the slower rise in salinity and inundation associated with SLR. At GWI and MS, after 2012, leaf properties declined rapidly as root mortality led to much lower  $\Psi_{\text{leaf}}$ , which forced stronger stomatal closure and significantly lowered photosynthesis and transpiration. The relative importance of ion toxicity and stomatal closure on leaf photosynthesis can be shown by the intrinsic water using efficiency (iWUE) (Fig. S5). The simulated iWUE of shoreline forest of all three sites is higher than upland forests indicating that stomatal closure constrains photosynthesis of shoreline trees. The pattern of simulated iWUEs is consistent with the observed patterns at all three sites (Wang *et al.*, 2019).

Consistent with the loss of function at the leaf level, whole-plant function also declined with seawater exposure (Fig. 4). Model outcomes show large reductions in % live crown, % NSC, and  $k/k_{\text{max}}$  in shoreline trees as compared to upland trees at all three sites, but as with the leaf-level responses, the changes are more rapid at BC than GWI and MS. Reduced xylem conductivity with increasing soil salinity has been observed in *Populus euphratica* (Rajput *et al.*, 2017) and in coastal mangrove forests (Reef & Lovelock, 2014; Méndez-Alonzo *et al.*, 2016). Also, canopy structure has been linked to the extent of sea water exposure in mangroves (Lovelock *et al.*, 2017). Our simulation reveals that at BC, %NSC and  $k/k_{\text{max}}$  decrease in the same manner; whereas at GWI and MS, the large loss of  $k/k_{\text{max}}$  occurs earlier than the drop in %NSC, which is more obvious at MS (Fig. 4). Unlike BC, where % NSC and % live crown decreased in concert with decreases in leaf GPP, loss of % NSC, % live crown, and  $k/k_{\text{max}}$  of shoreline forests at GWI and MS occurred in 2012, a few years later than leaf GPP started to decline in 2008. These changes at the Chesapeake Bay sites have two stages: a slight decrease in 2012 followed by a larger decrease since 2015 (Figs 3, 4). This is likely because the long-term chronic exposure to low salinity caused a slight reduction in photosynthesis capacity, which initially does not cause a large loss of carbon pools from the trees. The slight decrease in  $k/k_{\text{max}}$  in the earlier years is from increased osmotic potential in both soil water and sap, whereas the larger decline of  $k/k_{\text{max}}$  after 2015 is due to root mortality (Fig. 7). The larger decrease in  $k/k_{\text{max}}$  in later years further forced stomatal closure and caused a significant loss of leaf GPP, hence a reduction of % NSC and % live crown. Our simulated pattern of whole-plant functional loss supports the conceptual model of interacting water relation-based and carbon economy-based mechanisms (McDowell *et al.*, 2022).

Two major processes underlying coastal tree mortality include carbon starvation and hydraulic failure (McDowell *et al.*, 2022). The risk of carbon starvation increases with decreasing % NSC and the risk of hydraulic failure increases with decreasing  $k/k_{\text{max}}$ . The changes in the growth and mortality rates at the three sites examined in this study (Fig. 5) are the result of these processes. Trees first experience a loss of leaf GPP, that results in a lower growth rate. As the loss of leaf GPP and  $k/k_{\text{max}}$  resulting from

root mortality, ion toxicity, and loss of live crown becomes more significant, tree growth ceases and mortality increases. The simulated change in growth rate of both shoreline and upland trees at BC matches well with observations (Wang *et al.*, 2022). The simulated change in growth rate at the Chesapeake Bay sites was also consistent with observed patterns except the simulated growth rate at MS site is higher than observed rates (Fig. 5d,e).

The relative importance of carbon starvation vs hydraulic failure in total mortality differs among the three sites. The different scenarios of soil salinity variation at BC, and GWI and MS determine both the rate and the order of progress of the loss of NSC and  $k/k_{\text{max}}$  and hence the dominant process underlying mortality. The shoreline forest at BC experienced a sudden and large increase in soil salinity immediately after dam removal in late 2014. This caused a rapid loss of photosynthetic capacity and elevated root mortality because high salt concentrations result in more rapid enzyme degradation and root damage (Munns, 2002). Thus, both decreasing %NSC and loss of  $k/k_{\text{max}}$  occurred in the first year after sea water exposure, and carbon starvation and hydraulic failure relatively equally contribute to tree mortality. Over time, consumption of storage carbon for respiration further drives % NSC down, and the contribution of carbon starvation to total mortality increases (Fig. 8, purple line).

In contrast to BC, the shoreline trees at GWI and MS experienced chronic rises in salinity. The prolonged period of elevated soil salinity resulted in a slow decrease in photosynthetic capacity and root biomass. Because of the slow loss of leaf GPP, it required longer for the loss of storage carbon to occur. Both simulated and field observations of growth rate (Fig. 5c,e) indicate that it is not until 2015 that the shoreline trees at GWI and MS reach a negative carbon balance, and then it takes a number of years for the storage carbon to be depleted to a critically low value, resulting in mortality. On the other hand, trees start to experience hydraulic stress as soon as soil water potential decreases due to the change in osmotic potential, and the long-term cumulative effect of root loss. Therefore, the loss of  $k/k_{\text{max}}$  occurs earlier than the loss of %NSC, and consequently hydraulic failure is the major process underlying mortality at the Chesapeake Bay sites. Over time, the loss of photosynthesis capacity causes more rapid loss of storage carbon, and then carbon starvation increases. This is what happened at GWI in the last few years of the study (Fig. 8 blue line). At MS, soil salinity rose at a slower rate and we only see the increase in hydraulic failure mortality since 2015 (Fig. 8 green line).

Our study indicates that root mortality is an important mechanism in tree mortality, whereas changing vulnerability to embolism only has a noticeable impact on  $k/k_{\text{max}}$  under severe soil salinity and a minor effect in other cases (Figs 6, 7). The major effect of root mortality is the reduced total conductivity. Although we have no measurements of root mortality, our simulations indicate that root mortality did occur at shoreline forests because only the simulation with the root mortality mechanism active matches the iWUE and loss of xylem conductance (Figs 7, S6). The simulated  $k/k_{\text{max}}$  with and without root mortality indicates that root mortality is a major factor underlying hydraulic failure. Without root mortality, stomatal closure would be

sufficient to prevent excessive loss of xylem conductivity leading to hydraulic failure. However, root mortality greatly reduces total plant hydraulic conductance, thus even when the stomata close, transpirational water loss through the cuticle would result in significantly lower xylem water potential and greater embolism. At BC, both the changing vulnerability curve and root mortality were important for the loss of xylem conductivity and hydraulic failure. At GWI and MS, root mortality played a more important role in lowering xylem conductivity than changing vulnerability curves. Without root mortality, tree mortality at GWI starts to occur from 2016 from carbon starvation, but with root mortality, tree mortality rapidly increases after 2012 (Fig. 6h). At MS, without root mortality, the total mortality remains near zero over the entire period, but with root mortality, mortality driven by hydraulic failure started to increase after 2012. The effect of root mortality on hydraulic stress indicated by our simulation is consistent with previous studies (Zaerr, 1983; Pezeshki *et al.*, 1996). Reductions in  $g_s$  and total root conductivity in response to waterlogging are strongly correlated (Islam & Macdonald, 2004; Aroca *et al.*, 2011; Karlova *et al.*, 2021). This can be explained by the same mechanisms: root mortality increases whole-plant hydraulic resistance and hence lowers leaf water potential, which forces stomatal closure and increased embolism.

We note that multiple assumptions and remaining development tasks exist for the application of FATES-Hydro to simulating SLR-induced ghost forest formation. The model assumes that the change in photosynthetic capacity is instantaneous with a change in soil salinity. However, enzyme degradation may take days to months to occur (Munns, 2002) thus a lag may exist. We assumed similar functional responses to salinity between BC and MS and GWI; however, the conditions and species varied between BC and the two Chesapeake Bay sites. This means that the predictions for MS and GWI should be considered hypotheses rather than conclusions *per se*. From a plant functional type (Fisher *et al.*, 2018) perspective, this approach falls within the needleleaf conifer functional type, and both conifer species are relatively salt tolerant as they are common on their respective coasts (*Picea sitchensis* at BC and *Pinus taeda* at MS and GWI). Measurements at these sites are ongoing and will allow future testing of differences between species in model outcomes and how differences in traits may influence them.

Here, we incorporated the physiological effect of sea water exposure on conifer trees in a vegetation dynamic model, FATES-Hydro, and ran the model at three sites dominated by conifer trees. Our study reveals that the same underlying physiological mechanisms can lead to different mortality patterns in terms of the rate of mortality and the relative importance of carbon starvation and hydraulic failure. Specifically, we showed that the loss of xylem and photosynthetic functions can lead to rapid tree mortality from hydraulic failure and carbon starvation under sudden and severe sea water exposure, but slow and chronic seawater exposure forced a greater proportion of hydraulic failure dominated mortality. The newly developed FATES-Hydro is a mechanistic model based on first order physical principles. Once validated, the model can be used to examine the impacts of sea-level changes between gradual rises and sudden inundations on forest productivity and mortality,

as well as make projections of the impact of SLR on coastal ecosystems under future climate scenarios. By exploring both the likelihood and potential mechanisms of coastal forest mortality under different circumstances, this analysis benchmarks model performance while also providing directions for future study.

## Acknowledgements

JD, NM, BBL, NW, JPM, PR, SCP, MW, and VB were supported by the U.S. Department of Energy, Office of Biological and Environmental Research project Coastal Observations, Mechanisms, and Predictions Across Scales (COMPASS). Any use of trade, product, or firm names is for descriptive purposes only and does not imply endorsement by the U.S. Government. HZ acknowledges the support of the National Natural Science Foundation of China (grant nos. 32201289). MK acknowledges the support of the U.S. National Science Foundation (nos. 1654374, 1832221, 2012670).





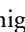




## Competing interests

None declared.

## Author contributions

JD and NM designed the study and drafted the manuscript. JD developed the model and performed the simulations. NW, MLK, PR, PZ, HZ, SCP, SW, WW, WI and AS collected field data and performed data analysis. All the authors contribute to write the manuscript and revision.

## ORCID

Vanessa Bailey  <https://orcid.org/0000-0002-2248-8890>  
 Junyan Ding  <https://orcid.org/0000-0002-0739-0545>  
 Weibin Li  <https://orcid.org/0000-0001-8970-0318>  
 Nate McDowell  <https://orcid.org/0000-0002-2178-2254>  
 Patrick Megonigal  <https://orcid.org/0000-0002-2018-7883>  
 Stephanie C. Pennington  <https://orcid.org/0000-0003-2685-1092>  
 Wenzhi Wang  <https://orcid.org/0000-0003-4574-409X>  
 Nicholas Ward  <https://orcid.org/0000-0001-6174-5581>  
 Hongxia Zhang  <https://orcid.org/0000-0002-8358-8617>

## Data availability

The data and FATES-Hydro code that support the findings of this study are openly available in github repository: [https://github.com/JunyanDing/FATES\\_COMPASS](https://github.com/JunyanDing/FATES_COMPASS).

## References

- Aroca R, Porcel R, Ruiz-Lozano JM. 2011. Regulation of root water uptake under abiotic stress conditions. *Journal of Experimental Botany* 63: 43–57.
- Ball MC, Farquhar GD, Box PO. 1984. Photosynthetic and stomatal responses of two mangrove species, *Aegiceras corniculatum* and *Avicennia marina*, to long term salinity and humidity conditions. *Plant Physiology* 74: 1–6.

- Chen Y, Kirwan ML. 2022a. A phenology- and trend-based approach for accurate mapping of sea-level driven coastal forest retreat. *Remote Sensing of Environment* 281: 113229.
- Chen Y, Kirwan ML. 2022b. Climate-driven decoupling of wetland and upland biomass trends on the mid-Atlantic coast. *Nature Geoscience* 15: 913–918.
- Christoffersen BO, Gloor M, Fauset S, Fyllas NM, Galbraith DR, Baker TR, Kruijt B, Rowland L, Fisher RA, Binks OJ *et al.* 2016. Linking hydraulic traits to tropical forest function in a size-structured and trait-driven model (TFS vol 1-Hydro). *Geoscientific Model Development* 9: 4227–4255.
- Clough BF, Sim RG. 1989. Changes in gas exchange characteristics and water use efficiency of mangroves in response to salinity and vapour pressure deficit. *Oecologia* 79: 38–44.
- Delatorre-herrera J, Ruiz KB, Pinto M. 2021. The importance of non-diffusional factors in determining photosynthesis of two contrasting quinoa ecotypes (*Chenopodium quinoa* Willd.) subjected to salinity conditions. *Plants* 10: 927.
- Duberstein JA, Krauss KW, Baldwin MJ, Allen ST, Conner WH, Salter JS, Miloshis M. 2020. Small gradients in salinity have large effects on stand water use in freshwater wetland forests. *Forest Ecology and Management* 473: 118308.
- Ezer T, Corlett WB. 2012. Is sea level rise accelerating in the Chesapeake Bay? A demonstration of a novel new approach for analyzing sea level data. *Geophysical Research Letters* 39: 744–755.
- Falster DS, Duursma RA, Ishihara MI, Barneche DR, Fitzjohn RG, Rhammar AV, Aiba M, Ando M, Anten N, Aspinwall MJ *et al.* 2015. BAAD: a biomass and allometry database for woody plants ecological archives E096-128. *Ecology* 96: 1445.
- Fisher RA, Koven CD, Anderegg WRL, Christoffersen BO, Dietze MC, Farrior CE, Holm JA, Hurtt GC, Knox RG, Lawrence PJ *et al.* 2018. Vegetation demographics in Earth system models: a review of progress and priorities. *Global Change Biology* 24: 35–54.
- Flexas J, Bota J, Loreto F, Cornic G, Sharkey TD. 2004. Diffusive and metabolic limitations to photosynthesis under drought and salinity in C3 plants. *Plant Biology* 6: 269–279.
- Flowers TJ, Colmer TD. 2008. Salinity tolerance in halophytes. *New Phytologist* 179: 945–963.
- Golaz JC, Van Roekel LP, Zheng X, Roberts AF, Wolfe JD, Lin W, Bradley AM, Tang Q, Maltrud ME, Forsyth RM *et al.* 2022. The DOE E3SM Model Version 2: overview of the physical model and initial model evaluation. *Journal of Advances in Modeling Earth Systems* 14: 1–51.
- Islam MA, Macdonald SE. 2004. Ecophysiological adaptations of black spruce (*Picea mariana*) and tamarack (*Larix laricina*) seedlings to flooding. *Trees – Structure and Function* 18: 35–42.
- Karlova R, Boer D, Hayes S, Testerink C. 2021. Root plasticity under abiotic stress. *Plant Physiology* 187: 1057–1070.
- Kattge J, Díaz S, Lavorel S, Prentice IC, Leadley P, Bönsch G, Garnier E, Westoby M, Reich PB, Wright IJ *et al.* 2011. TRY - a global database of plant traits. *Global Change Biology* 17: 2905–2935.
- Kauffman JB, Giovanonni L, Kelly J, Dunstan N, Borde A, Diefenderfer H, Cornu C, Janousek C, Apple J, Brophy L. 2020. Total ecosystem carbon stocks at the marine-terrestrial interface: Blue carbon of the Pacific Northwest Coast, United States. *Global Change Biology* 26: 5679–5692.
- Kirwan ML, Gedan KB. 2019. Sea-level driven land conversion and the formation of ghost forests. *Nature Climate Change* 9: 450–457.
- Koven CD, Knox RG, Fisher RA, Fisher RA, Chambers JQ, Chambers JQ, Christoffersen BO, Davies SJ, Detto M, Detto M *et al.* 2020. Benchmarking and parameter sensitivity of physiological and vegetation dynamics using the Functionally Assembled Terrestrial Ecosystem Simulator (FATES) at Barro Colorado Island, Panama. *Biogeosciences* 17: 3017–3044.
- Lawrence DM, Fisher RA, Koven CD, Oleson KW, Swenson SC, Bonan G, Collier N, Ghimire B, van Kampenhou L, Kennedy D *et al.* 2019. The Community Land Model Version 5: description of new features, benchmarking, and impact of forcing uncertainty. *Journal of Advances in Modeling Earth Systems* 11: 4245–4287.
- Li W, McDowell NG, Zhang H, Wang W, Mackay DS, Leff R, Zhang P, Ward ND, Norwood M, Yabusaki S *et al.* 2022. The influence of increasing atmospheric CO<sub>2</sub>, temperature, and vapor pressure deficit on seawater-induced tree mortality. *New Phytologist* 235: 1767–1779.
- Li W, Zhang H, Wang W, Zhang P, Ward ND, Norwood M, Myers-Pigg A, Zhao C, Leff R, Yabusaki S *et al.* 2021. Changes in carbon and nitrogen metabolism during seawater-induced mortality of *Picea sitchensis* trees. *Tree Physiology* 41: 2326–2340.
- López-Berenguer C, García-Viguera C, Carvajal M. 2006. Are root hydraulic conductivity responses to salinity controlled by aquaporins in broccoli plants? *Plant and Soil* 279: 13–23.
- Lovelock CE, Feller IC, Reef R, Hickey S, Ball MC. 2017. Mangrove dieback during fluctuating sea levels. *Scientific Reports* 7: 1680.
- Manzoni S. 2014. Integrating plant hydraulics and gas exchange along the drought-response trait spectrum. *Tree Physiology* 34: 1031–1034.
- McDowell NG, Ball M, Bond-Lamberty B, Kirwan ML, Krauss KW, Megonigal JP, Mencuccini M, Ward ND, Weintraub MN, Bailey V. 2022. Processes and mechanisms of coastal woody-plant mortality. *Global Change Biology* 28: 5881–5900.
- Méndez-Alonzo R, López-Portillo J, Moctezuma C, Bartlett MK, Sack L. 2016. Osmotic and hydraulic adjustment of mangrove saplings to extreme salinity. *Tree Physiology* 36: 1562–1572.
- Munns R. 2002. Comparative physiology of salt and water stress. *Plant, Cell & Environment* 25: 239–250.
- Munns R, Termaat A. 1986. Whole-plant responses to salinity. *Functional Plant Biology* 13: 143.
- Nedjimi B. 2014. Effects of salinity on growth, membrane permeability and root hydraulic conductivity in three saltbush species. *Biochemical Systematics and Ecology* 52: 4–13.
- Nishida K, Khan NM, Shiozawa S. 2009. Effects of salt accumulation on the leaf water potential and transpiration rate of pot-grown wheat with a controlled saline groundwater table. *Soil Science and Plant Nutrition* 55: 375–384.
- Oleson KW, Lawrence DM, Bonan GB, Drewniak B, Huang M, Koven CD, Samuel L, Fang L, Riley WJ, Subin ZM *et al.* 2013. Technical description of v.4.5 of the Community Land Model (CLM). *Natl. Cent. Atmos. Res. Tech. Note.* [WWW document] URL <https://opensky.ucar.edu/islandora/object/technotes:515> [accessed 13 May 2023].
- Orsini F, Alnayef M, Bona S, Maggio A, Gianquinto G. 2012. Low stomatal density and reduced transpiration facilitate strawberry adaptation to salinity. *Environmental and Experimental Botany* 81: 1–10.
- Osland MJ, Chivoiu B, Enwright NM, Thorne KM, Guntenpergen GR, Grace JB, Dale LL, Brooks W, Herold N, Day JW *et al.* 2022. Migration and transformation of coastal wetlands in response to rising seas. *Science Advances* 8: eabo5174.
- Pan X, Ye Z, Xu B, Jiang T, Yang J, Tian Y. 2020. Population connectivity in a highly migratory fish, Japanese Spanish mackerel (*Scomberomorus niphonius*), along the Chinese coast, implications from otolith chemistry. *Fisheries Research* 231: p. 105690.
- Perri S, Katul GG, Molini A. 2019. Xylem–phloem hydraulic coupling explains multiple osmoregulatory responses to salt stress. *New Phytologist* 224: 644–662.
- Pezeshki SR. 2001. Wetland plant responses to soil flooding. *Environmental and Experimental Botany* 46: 299–312.
- Pezeshki SR, Pardue JH, DeLaune RD. 1996. Leaf gas exchange and growth of flood-tolerant and flood-sensitive tree species under low soil redox conditions. *Tree Physiology* 16: 453–458.
- Qin J, Dong WY, He KN, Yu Y, Tan GD, Han L, Dong M, Zhang YY, Zhang D, Li AZ *et al.* 2010. NaCl salinity-induced changes in water status, ion contents and photosynthetic properties of *Shepherdia argentea* (Pursh) Nutt. seedlings. *Plant, Soil and Environment* 56: 325–332.
- Rajput VD, Yaning C, Ayup M, Minkina T, Sushkova S, Mandzhieva S. 2017. Physiological and hydrological changes in *Populus euphratica* seedlings under salinity stress. *Acta Ecologica Sinica* 37: 229–235.
- Reef R, Lovelock CE. 2014. Regulation of water balance in mangroves. *Annals of Botany* 115: 385–395.
- Regier P, Ward ND, Indivero J, Wiese Moore C, Norwood M, Myers-Pigg A. 2021. Biogeochemical control points of connectivity between a tidal creek and its floodplain. *Limnology and Oceanography Letters* 6: 134–142.
- Robin AHK, Matthew C, Uddin MJ, Bayazid KN. 2016. Salinity-induced reduction in root surface area and changes in major root and shoot traits at the phytomer level in wheat. *Journal of Experimental Botany* 67: 3719–3729.

- Sallenger AH Jr, Doran KS, Howd PA. 2012. Hotspot of accelerated sea-level rise on the Atlantic coast of North America. *Nature Climate Change* 2: 884–888.
- Schieder NW, Kirwan ML. 2019. Sea-level driven acceleration in coastal forest retreat. *Geology* 47: 1151–1155.
- Schieder NW, Walters DC, Kirwan ML. 2018. Massive upland to wetland conversion compensated for historical marsh loss in Chesapeake Bay, USA. *Estuaries and Coasts* 41: 940–951.
- Smith IM, Fiorino GE, Grabas GP, Wilcox DA. 2021. Wetland vegetation response to record-high Lake Ontario water levels. *Journal of Great Lakes Research* 47: 160–167.
- Smith AJ, Kirwan ML. 2021. Sea level-driven marsh migration results in rapid net loss of carbon. *Geophysical Research Letters* 48: e2021GL092420.
- Sperry JS, Adler FR, Campbell GS, Comstock JP. 1998. Limitation of plant water use by rhizosphere and xylem conductance: results from a model. *Plant, Cell & Environment* 21: 347–359.
- Sperry JS, Wang Y, Wolfe BT, Mackay DS, Anderegg WRL, McDowell NG, Pockman WT. 2016. Pragmatic hydraulic theory predicts stomatal responses to climatic water deficits. *New Phytologist* 212: 577–589.
- Suárez N, Medina E. 2006. Influence of salinity on Na<sup>+</sup> and K<sup>+</sup> accumulation, and gas exchange in *Avicennia germinans*. *Photosynthetica* 44: 268–274.
- Sudhir P, Murthy SDS. 2004. Effects of salt stress on basic processes of photosynthesis. *Photosynthetica* 42: 481–486.
- Tagestad J, Ward ND, Butman D, Stegen J. 2021. Small streams dominate US tidal reaches and will be disproportionately impacted by sea-level rise. *Science of the Total Environment* 753: 141944.
- Tobin B, Black K, Osborne B, Reidy B, Bolger T, Nieuwenhuis M. 2006. Assessment of allometric algorithms for estimating leaf biomass, leaf area index and litter fall in different-aged Sitka spruce forests. *Forestry* 79: 453–465.
- University of East Anglia Climatic Research Unit, Harris IC. 2019. *CRU JRA: Collection of CRU JRA forcing datasets of gridded land surface blend of Climatic Research Unit (CRU) and Japanese reanalysis (JRA) data*. [WWW document] URL <https://catalogue.ceda.ac.uk/uuid/863a47a6d8414b6982e1396c69a9efc8> [accessed 8 October 2022].
- Wang W, McDowell NG, Ward ND, Indivero J, Gunn C, Bailey VL. 2019. Constrained tree growth and gas exchange of seawater-exposed forests in the Pacific Northwest, USA. *Journal of Ecology* 107: 2541–2552.
- Wang W, Zhang P, Zhang H, Grossiord C, Pennington SC, Norwood MJ, Li W, Pivovarov AL, Fernández-De-Uña L, Leff R *et al.* 2022. Severe declines in hydraulic capacity and associated carbon starvation drive mortality in seawater exposed Sitka-spruce (*Picea sitchensis*) trees. *Environmental Research Communications* 4: 35005.
- Ward ND, Patrick Megonigal J, Bond-Lamberty B, Bailey VL, Butman D, Canuel EA, Diefenderfer H, Ganju NK, Goñi MA, Graham EB *et al.* 2020. Representing the function and sensitivity of coastal interfaces in Earth system models. *Nature Communications* 11: 1–14.
- Yabusaki SB, Myers-Pigg AN, Ward ND, Waichler SR, Sengupta A, Hou Z, Chen X, Fang Y, Duan Z, Serkowski JA *et al.* 2020. Floodplain inundation and salinization from a recently restored first-order tidal stream. *Water Resources Research* 56: e2019WR026850.
- Yadav S, Irfan M, Ahmad A, Hayat S. 2011. Causes of salinity and plant manifestations to salt stress: a review. *Journal of environmental biology. Journal of Environmental Biology* 32: 667–685.
- Yoshikai M, Nakamura T, Suwa R, Sharma S, Rollon R, Yasuoka J, Egawa R, Nadaoka K. 2022. Predicting mangrove forest dynamics across a soil salinity gradient using an individual-based vegetation model linked with plant hydraulics. *Biogeosciences* 19: 1813–1832.
- Zaerr JB. 1983. Short-term flooding and net photosynthesis in seedlings of three conifers. *Forest Science* 29: 71–78.
- Zeng X. 2001. Global vegetation root distribution for land modeling. *Journal of Hydrometeorology* 2: 525–530.
- Zhang H, Li X, Wang W, Pivovarov AL, Li W, Zhang P, Ward ND, Myers-Pigg A, Adams HD, Leff R *et al.* 2021. Seawater exposure causes hydraulic damage in dying Sitka-spruce trees. *Plant Physiology* 187: 873–885.
- Zhang P, McDowell NG, Zhou X, Wang W, Leff RT, Pivovarov AL, Zhang H, Chow PS, Ward ND, Indivero J *et al.* 2021. Declining carbohydrate content of Sitka-spruce trees dying from seawater exposure. *Plant Physiology* 185: 1682–1696.

## Supporting Information

Additional Supporting Information may be found online in the Supporting Information section at the end of the article.

**Fig. S1** Major model development: change in photosynthetic capacity with leaf salinity, change in vulnerability curve with xylem salinity, and root loss from cumulative soil salinity and hypoxia.

**Fig. S2** Modeled soil salinity of the 22 tree locations at BC; open water salinity of station LE4.3, GWI and station ET5.2 MS; spot measurement of soil salinity of GWI and MS, colored solid lines are open water salinity of the corresponding time.

**Fig. S3** Comparison of empirically estimated soil salinity and measured soil salinity at the shoreline locations of Goodwin island and Money stump.

**Fig. S4** Comparison of  $V_{cmax}$  and SLA of Beaver Creek and Cheasepeak Bay site; boxes represent the 75<sup>th</sup> and 25<sup>th</sup> percentiles of the data, and whiskers are the 90<sup>th</sup> and 10<sup>th</sup> percentiles.

**Fig. S5** Effects on leaf hydraulic conditions. Annual mean intrinsic water using efficiency at BC, GWI, and MS. Mean monthly leaf water potential at BC, GWI, and MS.

**Fig. S6** Additional figures on effect of individual mechanism of root mortality (R.M.) and change in vulnerability curve (C. Vul) at shoreline forests. Annual mean intrinsic water using efficiency at BC, GWI, and MS. Mean monthly % live crown at BC, GWI, and MS. Annual growth rate at BC, GWI, and MS.

**Methods S1** FATES-Hydro model development.

**Methods S2** Create soil salinity for GWI and MS from open water salinity.

Please note: Wiley is not responsible for the content or functionality of any Supporting Information supplied by the authors. Any queries (other than missing material) should be directed to the *New Phytologist* Central Office.